

PAPER

Reduced graphene oxide-modified electrodes via fused deposition modeling 3D printing for hydrogen peroxide sensor

To cite this article: Yan Dou et al 2024 2D Mater. 11 045008

View the article online for updates and enhancements.

You may also like

- A comprehensive review of atomically thin silicates and their applications
 Preeti Lata Mahapatra, Gelu Costin, Douglas S Galvao et al.
- A review on transfer methods of twodimensional materials I Cheliotis and I Zergioti
- <u>When 2D materials meet metals</u> Luka Pirker, Jan Honolka, Matj Velický et al

2D Materials



20 June 2024

REVISED

5 July 2024

ACCEPTED FOR PUBLICATION 30 July 2024

PUBLISHED

9 August 2024

PAPER

Reduced graphene oxide-modified electrodes via fused deposition modeling 3D printing for hydrogen peroxide sensor

Yan Dou¹, Rui Dai¹, Haofan Sun¹, Kun Bi¹, Xin Zhao² and Qiong Nian^{1,*}

- School of Engineering for Matter, Transport and Energy, Arizona State University, Tempe, AZ, United States of America
- Department of Mechanical Engineering, Clemson University, Clemson, SC, United States of America
- Author to whom any correspondence should be addressed.

E-mail: Qiong.Nian@asu.edu

Keywords: 3D printed electrochemical sensors, dual-extrusion 3D printing, surface modification with graphene, hydrogen peroxide detection

Supplementary material for this article is available online

Abstract

Fused deposition modeling 3D printing provides a cost-effective and streamlined method for producing electrochemical sensors, overcoming the challenges associated with material selection, complex fabrication processes, and reproducibility issues. This study introduces an innovative approach utilizing a dual-printer setup to simplify the manufacturing of sensor electrodes. A critical enhancement in this process is the surface modification with reduced graphene oxide (rGO), which not only improves the electrochemical characteristics but also induces a wrinkled structure on the 3D printed surface. These wrinkles significantly increase the surface area, directly boosting the electrode's electrochemical performance. Comprehensive characterization of the electrode surfaces, both before and after rGO modification, demonstrates a substantial increase in sensitivity, with a fortyfold improvement observed in hydrogen peroxide (H_2O_2) amperometric measurements. This breakthrough paves the way for advanced applications in 3D printed electrochemical sensors.

1. Introduction

Electrochemical sensors are devices that detect the presence or concentration of a target analyte using electrical signals. They comprise a working electrode where the analyte undergoes a reaction, a reference electrode for stable potential, and a counter electrode to complete the circuit. These electrodes are immersed in an electrolyte that facilitates ion movement. A transducer in the sensor converts the chemical signal to an electrical one, which is then amplified and processed to determine the analyte's concentration. Based on this principle, the electrochemical sensors are widely used in a range of applications, including glucose sensors [1, 2], environmental monitoring [3, 4], food safety testing [5, 6], medical diagnostics [7, 8], and industrial process control [9, 10]. Although these applications are attractive, the manufacturing process for electrochemical sensors is still full of challenges.

The manufacturing methods for electrochemical sensors vary depending on the type of sensor and the materials used. One method is patterning process like chemical vapor deposition (CVD), lithography, laser-induced graphene (LIG) and electrochemical reduction from graphene oxide (GO) [11, 12]. CVD-synthesized nanomaterial's (metal oxides [13, 14] or 2D materials [15, 16]) often require pre-patterning a surface with a metallic catalyst to trigger layer deposition. And the desired materials always grow within a high temperature (up to 1000 °C), low-pressure vacuum environment injected with precursor gases. Hence, this method has found limitations in its high cost, inadequate scalability, and extreme process requirements. For lithography technology, it is a powerful method for fabricating electrochemical sensors with micro- and nanoscale structures [17]. However, creating the photomask that defines the pattern to be transferred onto the substrate is complex and time-consuming [18]. LIG has gained widespread attention for its rapid, cost-effective, laser assisted maskless production. It typically results in multi-layered porous graphene structures with high electrochemical activity on flat

polyimide substrate or phenolic resins, while the resulting structure may have limited mechanical strength [19]. In addition, the electrochemical reduction of GO represents an energy-efficient method for fabricating graphene sensor electrodes. The resulting electrochemically reduced GO electrodes can be utilized in various sensing applications. In recent years, solution-phase printing methods for producing electrochemical sensors are beginning to emerge, including inkjet printing [20, 21], screen printing [22, 23], and spray coating [24]. In general, solution-phase printing techniques use dispersion solvents and polymer additives in the ink, thus require post-print processing, such as thermal [25, 26], laser [27, 28], or photonic annealing [29, 30], to remove undesired polymer additives and enhance electrical conductivity. But, annealing or curing at high temperatures [31] potentially damages the paper substrates or thermally sensitive polymer substrate. While these existing fabrication methods for electrochemical sensors are wellestablished, they are mainly designed for making 2D sensors and may not be suitable for producing 3D sensors. The advantages of 3D electrochemical sensors over 2D counterparts lie in their enhanced surface area, improved mass transport properties and greater versatility in design. Therefore, studying the fabrication process of 3D electrochemical sensors is highly meaningful.

The advent of 3D printed electrodes has opened up new possibilities for applicability in diverse sectors such as biomedical engineering [32, 33], environmental monitoring [34, 35], and energy storage [36, 37]. Additive manufacturing stands out as the predominant 3D printing technique. Its integration into the realm of electrochemical sensor manufacturing has unveiled promising prospects for on-demand sensor fabrication and the realization of novel threedimensional sensor designs [38, 39]. Fused deposition modeling (FDM) is one of the most used 3D printing techniques, which is based on melting polymeric filaments, then extruding and depositing them onto 3D structure. By controlling the printing parameters, the morphological and structural characteristics of printed electrochemical devices or sensors can be modulated. For example, Hamzah et al reported a mini review on using 3D printing to fabricate electrodes in different geometries, sizes, and morphologies [40]. On the other hand, the choice of printable materials also plays a vital role in determining the performance of the 3D printed devices. In prior reports, conductive polymer filaments containing carbon black particles [41, 42], carbon nanofibers [43, 44], and graphite microparticles [45, 46] are usually used for the FDM 3D printing of electrochemical sensors and biosensors due to the high conductivity of carbon fillers and good biocompatibility of the polymer matrix [47]. However, these printed sensors typically exhibit unsatisfactory electrical conductivity or

electrochemical sensitivity [48], attribute to the fact that these conductive filaments generally contain a large fraction of non-conductive thermoplastics (e.g. ABS and PLA) while only a small fraction of conductive fillers (e.g. carbon allotropes) to maintain acceptable FDM printability.

This paper reports a novel method that can overcome the limits of the current 3D printed sensor electrodes to achieve superior sensitivity. Instead of choosing the carbon filled filament, we select a filament containing nanosized metals with 5 times or higher electrical conductivity [49]. The focus is on printing electrodes with excellent conductivity and then imparting electrochemical activity by modifying the electrode surface. We use a dual extruder printer to print both the conductive and encapsulation materials, enabling the integration of electrode encapsulation and batch production. After printing, a coating of rGO (using aqueous solution, no additives) is applied onto the surface for electrode modification, which allows the entire electrode to have excellent electrical conductivity and simultaneously desired electrochemical activity on the surface. Additionally, the specific surface area of the rGO modified electrode is significantly increased as the rGO flakes are coated on the FDM printing paths and thereby forming rough surface. This 3D printing morphology feature is further confirmed by microscopic observations. A favorable H₂O₂ sensing is also displayed by this scalable, 3D structuring of the rGO modified electrode without any additional post-printing processing steps.

2. Materials and methods

2.1. Materials

A commercial conductive filament (electrifi, Multi3D. Inc) in diameter of 1.75 mm is purchased to print the sensor electrodes. The supplier reports the resistivity of the filament as $0.006~\Omega$ -cm. To print the insulating packaging for the electrodes, a blue color Polylactic acid (PLA) filament in diameter of 1.75 mm, are purchased from Creality 3D Inc. The 3D printer utilized to print the above filaments is Creality Ender-3 pro (Creality 3D. Inc). The printer is upgraded from a single extruder to a dual extruder (Ender IDEX) using the extra parts supplied by SEN 3D. Inc for simultaneous printing and packaging of electrodes. Both nozzles of the dual extruder are in a diameter of 0.4 mm.

For surface modification of the 3D printed electrodes, rGO is prepared from a commercially available 4 mg ml⁻¹ graphene oxide water dispersion supplied by Graphenea with an improved subsequent reduction. Briefly, the graphene oxide suspension is diluted to 10 ml with a concentration of 0.25 mg ml⁻¹. After ultrasonication within 10 min, the diluted dispersion turns dark brown, then add

 $100~\mu l$ of ammonia hydroxide (10% v/v aq. Soln., Alfa Aesar) and 2 μl of hydrazine monohydrate (99+ %, Alfa Aesar) into the obtained brown dispersion and shake it vigorously for a few minutes. The dispersion is sealed and put into a 95 °C water bath for 1 h. During the water bath, the dark brown dispersion turns black. Afterward, the resulting black dispersion is cooled down and a precipitation layer floating on the surface of the dispersion is removed to obtain rGO aqueous solution. In addition, 0.5 ml of Nafion (5 wt.% in water, Aldrich) is added into the rGO aqueous solution.

2.2. Fabrication of rGO modified sensors

Using Computer-aided design software SOLIDWORKS, the full-size models of the electrodes with external packaging are created and saved as single stereolithography (STL) files. Then, the STL models are sliced into multiple layers to generate G-code files by using the slicing software Ultimaker Cura. After that, the G-code files are input into the 3D printer with a dual extruder to command the printing of the electrodes with external packaging. The electrodes are printed using the conductive filament at an extrusion temperature of 175 °C. The external packaging is printed using the blue PLA filament at an extrusion temperature of 210 °C. And all filaments are printed with a layer height of 0.15 mm, line width of 0.4 mm, and infill density of 100% with bed temperature of 60 °C. Printing time for a complete electrode is only 10 min with a printing speed of 30 mm s $^{-1}$.

After printing, a quantitative amount of rGO aqueous solution is aspirated by using a pipette gun and dropped onto the active surface of electrodes. Under the action of surface tension, a water droplet is formed and adsorbed on the active surface of electrodes. Then, the drop coated sensor electrodes are put into a vacuum chamber and dried. After vacuum drying, a series of rGO modified sensors with different mass loading are received. Herein, to determine the optimal rGO titration mass, electrodes were prepared with various rGO loadings, including 10, 20, 30, 40, 80 g, and 120 μ g.

2.3. Scanning electron microscopy of rGO modified electrodes and roughness measurements

The microstructures of electrode surfaces with and without rGO modification are investigated using a Field Emission Scanning Microscope (FEI Nova 200 NanoLab, Thermo Fischer. Inc.) The FE-SEM images are taken in secondary electron mode using 5 kV accelerating voltage and 1.6 nA beam current with a sample working distance of 5 mm from the field emitter source aperture. In addition, an (EDS) detector is used to determine the chemical compositions and distribution. For surface roughness testing, the 3D printed electrode surface and rGO modified surface are measured by Wide-area 3D measurement VR-3200 (Keyence corporation).

2.4. Raman spectroscopy and x-ray photoelectron spectroscopy of rGO modified electrodes

Confocal Raman microscope micrographs are obtained with an Acton 300 LN2 spectrometer and the signal is discriminated from the laser excitation using an Ondax SureBlock™ ultranarrow-band notch filter combined with two optigrate notch filters. The samples are detected using a 150 mW Coherent Sapphire SF laser with a 532 nm laser wavelength. The XPS spectrum of the electrode surfaces are also acquired using a Kratos Axis Supra+xray Photoelectron Spectrometer equipped with dual monochromatic Al/Ag source (Al K-alpha 1486.6 eV & Ag L-alpha 2984.2 eV). The binding energy survey scan was generated by measuring photoelectron energies from the constituent elements and subtracting the excitation energy.

2.5. Electrochemical testing and hydrogen peroxide sensing

Cyclic voltammetry test and amperometric H₂O₂ sensing are performed from a 3-electrode setup electrically connected to a CHI instrument potentiostat (660 series). The rGO modified sensor acted as the working electrode, Ag/AgCl (1M KCl) worked as the reference electrode, and a platinum wire worked as the counter electrode. For CV tests, the electrolyte of 5 mM K₃[Fe (CN)₆] and 0.1 M KCl is used to test the electrochemical activity. The rGO sensor is tested with the following five different CV scan rates: 5, 10, 20, 50, 100 mV s $^{-1}$. For H_2O_2 sensing, all electrodes are submerged in a test vial of 10 ml of 1X phosphate-buffered saline (PBS) with concentration of 137 mM NaCl, 10 mM phosphate, 2.7 mM KCl; pH 7.4, and the solution is continuously stirred (600 rpm) with a 0.5 cm (length) magnetic stir bar. Incremental increases in hydrogen peroxide concentration are achieved by pipetting 10 μ l of H₂O₂ in the test bottle ten times from 100 mM H₂O₂ solution. A working potential of 0.1 V between the working and counter electrodes is maintained during experiments. In addition, electrochemical impedance spectroscopy (EIS) is performed at the open-circuit voltage from 1 MHz to 1 Hz at the amplitude of 5 mV in 1X phosphate buffer solution.

3. Results and discussion

3.1. The manufacturing of the rGO modified 3D printed sensor

Figure 1 illustrates the proposed FDM 3D printing process to fabricate the aforementioned rGO modified electrode for efficient electrochemical sensor manufacturing. The principle of designing and printing the sensor electrode is straightforward, which relies on printing of both conductive filament into electrode and insulating filament into external packaging, by using the 3D printer with dual extruder. Figure 1(a) provides a schematic depiction of the

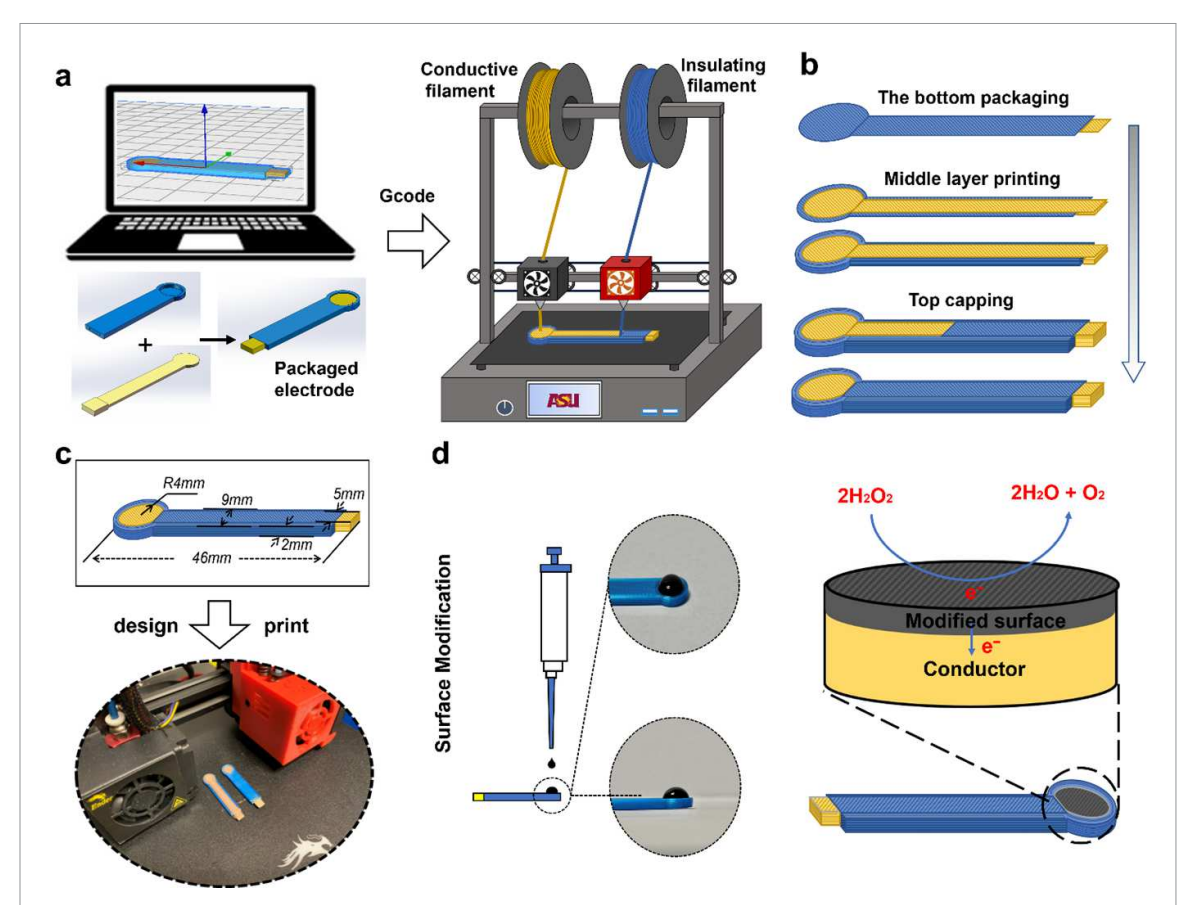


Figure 1. (a) Schematic diagram of modeling, printing and encapsulating electrodes using a dual extruder 3D printer. (b) The encapsulation process of the electrode from different printed layers. (c) The designed model and photograph of printed of the 3D printed electrode (d) Schematic representation of surface-modified sensor electrode.

dual extruder's operation, illustrating the simultaneous, single-step co-printing of both conductive (yellow color mark) and insulating (blue color mark) filaments, in alignment with the electrode model design. Note that the printing parameters of the two extruders (e.g. extruder temperature, infill density, infill pattern, printing speed, etc) can be independently controlled to optimize the quality of electrode and packaging each. Figure 1(b) shows the detailed procedure of the co-printing of sensor electrode. In detail, the entire co-printing process can be divided into three steps: the bottom packaging, middle layer printing, and top capping. At the beginning of the printing process, several layers of insulated filament are printed as the bottom packaging. These layers should be printed smoothly and should have good adhesiveness with the conductive filament, since they will be used as the substrate for printing conductive filaments in intermediate layers. Then, in the process of printing intermediate layers, each layer of conductive material is printed with the surrounding area wrapped by the insulated materials simultaneously to ensure sealing. During the final capping process, several layers of the insulated filament are printed again to expose a defined circular area of conductive material, in preparation for subsequent rGO drop casting.

The overall geometrical design and sizes are marked in figure 1(c) top. The sensor electrode designed is a single-channel electrode (yellow color mark) encased in a PLA package (blue color mark), as shown in figure 1(c). The single-channel electrode has a length of 45 mm, width of 5 mm, and thickness of 1 mm, while the package has a thickness of 0.5 mm that not only seals the electrodes but also defines the active area of the sensor. The geometrical surface area is \sim 50 mm² with a radius of 4 mm.

The electrode design above is then printed using our dual extruder printer and their photos are shown in the lower section figure 1(c). Noteworthy, during electrodes printing, the choice of printed materials, the printing temperature, and the infill pattern have significant impacts on the final electrode performance. The conductive filament chosen for this study comprises a metal composite, primarily containing silver and copper, intertwined with biodegradable polyester [53]. The measured resistivity of this composite is approximately 0.34 Ω ·cm. It is critical that the selected electrode materials maintain substantial conductivity subsequent to the printing process. A lack of sufficient conductivity would compromise the electrodes' ability to propagate electrical signals effectively. The printing process is executed at a minimum printable temperature of 175 °C.

2D Mater. 11 (2024) 045008 Y Dou et al

Table 1. The volume resistivity of different conductive filaments and corresponding works in 3D printed electrode.

Material	Composition	Volume resistivity (Ω -cm)	Corresponding works in 3D printed electrodes
Proto pasta	PLA/Carbon black	6.02-10.25	[41, 50]
Black magic	PLA/Graphene	0.6-2.59	[39, 51, 52]
Electrifi	Polyester/copper	0.34–1.65	This work

(A temperature notably higher than the recommended range of 140 °C-160 °C [49]. This increase is necessitated by the narrow heating zone of the 3D printer.) Post-printing, the resistivity escalates to 1.65 Ω ·cm for the printed electrodes. Regarding the insulating filaments, PLA is chosen for the electrode and it is employed to encapsulate the electrodes at a printing temperature of 210 °C. As for the infill pattern, all the electrodes and packaging are printed with a 100% infill density. The lines are patterned in one direction, either along the X- or Y-axis, on alternating layers. This expedited printing pattern not only economizes on material usage but also ensures the maintenance of electrical conductivity. Upon completion of the printing process, the 2-terminal resistance measured from the active area of the electrode to the back contact is roughly 150 Ω . As depicted in table 1, the selected electrode printing material utilized in this study exhibits lower resistivity compared to previous 3D printing materials, thereby ensuring effective transmission of electrical signals.

In addition to the high electrical conductivity, desired electrochemical activity is also of critical importance to pursue the sensor electrode with optimal sensing capabilities. To realize the desired electrochemical activity, we implement a surface modification process using rGO drop casting as shown in figure 1(d) after the electrode printing. This casting approach is considerably simpler and more effective than alternative surface processing methods. rGO suspensions are straightforward to prepare [54] and, given their exceptional performance, have been the subject of considerable research in the field of graphene-based sensors [55]. The entire rGO suspension drop coating process is conducted in a vacuum, thus efficiently preventing the metal elements on the electrode surface from reacting with oxygen and carbon dioxide in moist air. The rGO is chosen herein as one example though other materials can be used as well, such as currently well explored CNT [56], MXene [57], nanometals [58], conductive polymers [59], enzymes [60], etc. Another reason to choose rGO is that past research has furnished evidence supporting the significant catalytic impact of graphene-based biosensors on the redox reactions involving hydrogen peroxide, a transducer that plays a pivotal role in biological processes and serves as an essential chemical reagent in numerous industrial applications [61].

As shown in figure 1(d) right, following the application of the rGO casting, the sensor electrode successfully acquires its sensing capabilities with the graphene surface serves as a catalyst reducing the hydrogen peroxide to water and oxygen. Throughout this transformation, the electrons derived from the reduction process traverse the rGO layers and are subsequently transmuted into electrical signals at the electrode site.

3.2. Seal integrity testing of PLA packaging

In the context of electrode fabrication, an essential consideration pertains to the quality of the sealing process. The challenge of electrolyte leakage poses a significant hurdle, particularly in FDM printed structures, where inherent gaps exist between adjacent printed lines and layers. However, by precise control over nozzle size and layer thickness, it becomes feasible to manage the spacing between neighboring plastic strands [62]. In this study, a nozzle size of 0.4 mm and a layer height of 0.15 mm are employed for the entire electrode printing process. Consequently, instead of retaining its cylindrical form, the molten filament extruded undergoes plastic deformation, resulting in an oval cross-section. This transformation leads to an increased contact area, thereby enhancing filament fusion [63]. Figure 2(a) provides a cross-sectional depiction of the electrode, accurately embodying the distinctive printing characteristics inherent to the sensor electrode. The design specifications have been meticulously adhered to, with the insulating PLA sheath completely enveloping the electrodes (figure 2(a) top photo), offering a significant level of encapsulation. The scanning electron microscope (SEM) cross-sectional image (figure 2(a) bottom) of the electrode reveals an intricate layered printing structure. Each distinct layer stands at an approximate height of 150 μ m, which is defined by the 3D printing layer thickness. The interlayer connectivity is characterized by a close bonding between layers, a feature that is critical for maintaining the overall conductivity of the electrode.

To further test the quality of the sealing, an unpackaged electrode and a fully packaged electrode were individually immersed in a 1X PBS solution for a duration of 30 min. Subsequently, both electrodes were subjected to an anodic potential of 0.5 V for a specific time period. The efficacy of the sealing process during encapsulation was assessed by observing

2D Mater. 11 (2024) 045008 Y Dou et al

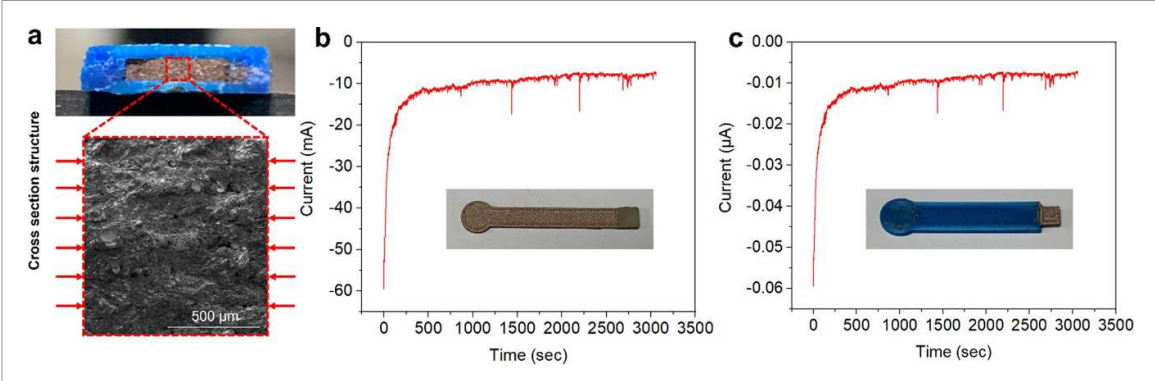


Figure 2. (a) The cross-sectional layered structure of the electrode. The oxidation currents of (b) unpackaged electrode and (c) fully packaged electrode by applying an anodic potential with 0.5 V over 3000 s.

and comparing the oxidation currents between the unpackaged and fully encapsulated electrodes. The results revealed a substantial contrast in oxidation currents, with the unpackaged electrode registering approximately 10 mA (figure 2(b)), whereas the fully encapsulated electrode exhibited a significantly lower oxidation current of approximately 0.01 μ A (figure 2(c)). This substantial disparity in oxidation currents underscores the excellent sealing quality achieved through the employed FDM printing process, effectively mitigating the risk of electrolyte leakage.

3.3. Surface morphological alterations before and after rGO modification

To comprehend the microstructural transformation from the surface of printed electrodes to the rGO modified surface, an initial analysis of the printed electrode surface morphology is conducted using SEM (figure 3(a)). The electrode surface exhibits overlapping line-by-line features on a 400 μ m scale. These features are a direct result of the line infill 3D printing process, which prints lines in one direction on alternate layers. The width of each line is approximately 485 μ m, and each line exhibits a rough and scoriaceous surface texture. The SEM image, at a 40 μ m scale, provides a clearer view of these features, revealing their relative roughness and microholes. Hence, it can be inferred that 3D printing contributes a degree of roughness to the electrode surface. Furthermore, the morphology of the rGO drop coated electrode surfaces is investigated using SEM at different mass loadings, and a significant correlation with the 3D-printed electrode surfaces is observed (figure 3(b)). The SEM images revealed that the microstructure of the rGO modified electrode surfaces consisted of continuous sheets of rGO covering the numerous micro holes. The presence of the rough printed lines led to various topological imperfections on the rGO sheets, such as wrinkles and ridges. These imperfections are visible in the SEM images at a 400 μ m scale. When examining the SEM images at a 40 μ m scale, it becomes more clearly observed that

the rGO modified electrode surface exhibited a higher density of wrinkles and ridges. Concurrently, near the areas with wrinkles, irregular holes with a diameter of $1-5~\mu m$ can be observed. This phenomenon is likely a result of the distortion of thin rGO films occurring during the evaporation of the rGO aqueous solution on the rough printed surface. Additionally, the morphology of the rGO modified surface can be better visualized by examining it cross-section (figure 3(c)). It is evident that the layers of rGO sheets envelop the undulating printed substrate, thereby increasing the specific surface area of the rGO modified electrode surface.

3.4. Surface composition alterations before and after rGO modification

Upon completion of the printing process, the elemental distribution on the 3D printed electrode surface is evaluated using EDS mapping. As depicted in figure 4(a), the elements carbon (C), copper (Cu), and silver (Ag) are found to be uniformly dispersed across the entire surface. This uniformity is a consequence of the metal-polymer composite nature of the conductive filament, which primarily consists of biodegradable polyester and copper [53]. Quantitative analysis revealed that the elemental mass ratios of carbon, copper, and silver on the electrode surfaces are approximately 56.44%, 26.05%, and 3.95%, respectively. These proportions of uniformly distributed and well-connected copper and silver are crucial for ensuring electrode conductivity. Moreover, the substantial quantity of carbon connects copper and silver as bonders in the form of thermoplastic polyester.

Subsequent to the observations, Raman spectroscopy is employed to characterize the microstructure of the rGO modified surfaces (figure 4(b)). Contrary to the 3D printed electrode surface, the Raman spectra of the rGO modified surfaces revealed D, G, and 2D peaks. These peaks, manifesting in distinct ranges, provide valuable information regarding the structure of graphene. Specifically, the D peak (~1336 cm⁻¹) signifies the disordered vibrational

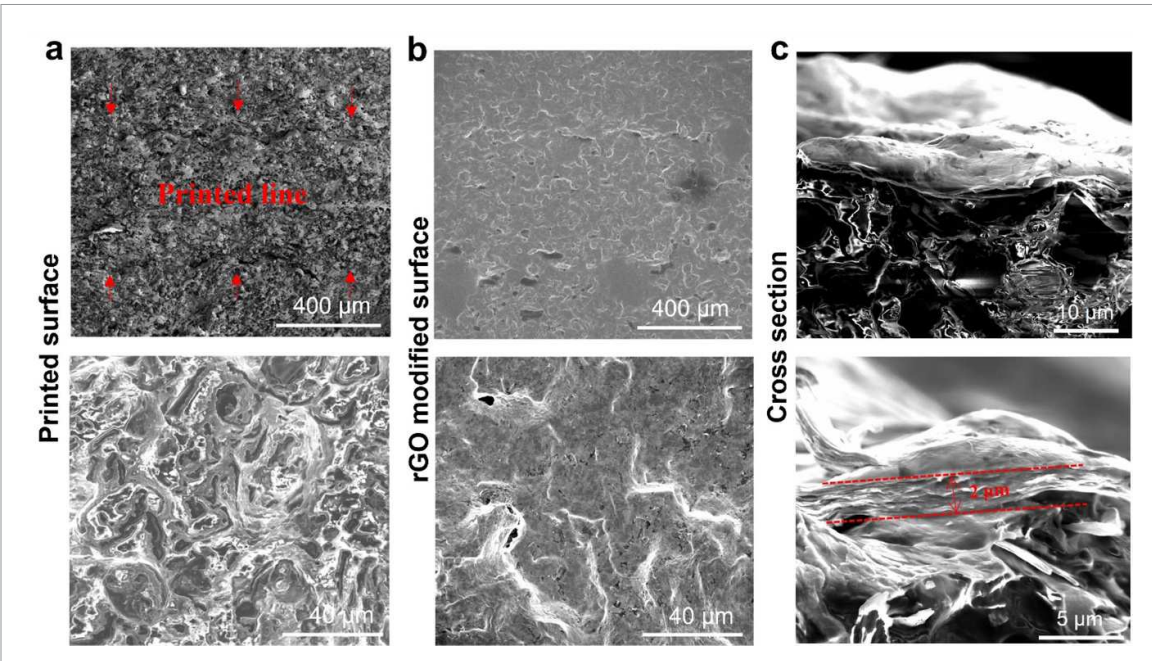


Figure 3. Scanning electron microscopy images of (a) the 3D printed surface without rGO modified and (b) with rGO modified surface respectively, and (c) the cross section of the rGO modified 3D printed electrodes.

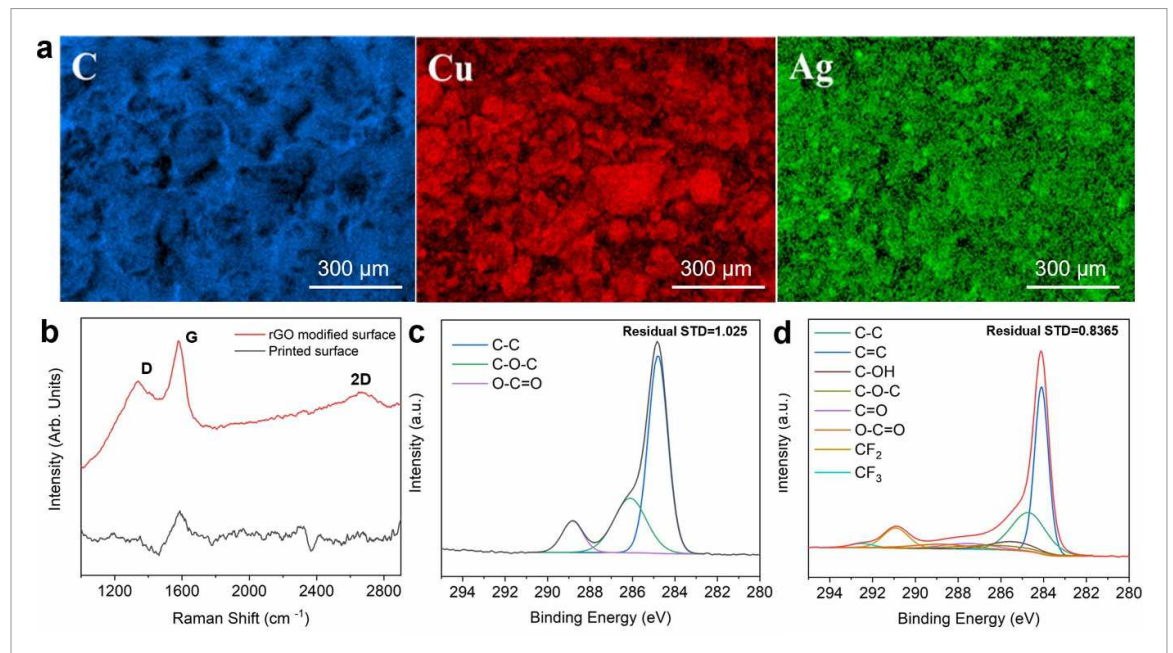


Figure 4. (a) The SEM image of 3D printed electrode surface, and corresponding quantitative EDS element mapping of *C*, Ag and Cu. (b) Raman spectra of 3D printed electrode surface and with rGO modified electrode surface. XPS graphs of (c) 3D printed electrode surface and with (d) rGO modified electrode surface.

peak of graphene; the G peak (\sim 1585 cm⁻¹) is indicative of the in-plane vibration of carbon atoms; and the 2D peak (\sim 2690 cm⁻¹) represents a two-phonon resonance Raman peak [64]. It is noteworthy that the 2D peak is particularly sensitive to the stacking of graphene layers. Consequently, it can be utilized to ascertain the number of graphene layers (be it monolayer, double layer, or multilayer). Given that the 2D peak of monolayer graphene characteristically emerges at 2679 cm⁻¹ and presents a well-defined

single Lorentzian peak pattern, the observed shift in position of the 2D peak combined with the full width at half maximum analysis infer that the rGO coating on the electrode comprises multiple layers. Furthermore, the shift in the 2D peak position can be attributed to residual oxygen-containing functional groups remaining post the reduction of GO to rGO [65]. The $\rm I_D/I_G$ ratio for rGO, as derived from the Raman spectra, approximates 1.04. This indicates the presence of disordered edge states in rGO modified

surfaces [66]. Such disorder facilitates a larger contact area with the electrolyte and exposes a greater number of electrochemical reaction active sites [67].

C 1 s XPS spectra are acquired for both the 3D printed surface and the rGO modified surface to assess changes in chemical states and the presence of functional groups. The C 1 s peak for both surfaces are subjected to analysis through deconvolution using Lorenzian peak fitting to identify constituent peaks. The 3D printed surface (figure 4(c)) displays the presence of ester functional groups in polyester, as indicated by the presence of C-O-C at 286.1 eV and O-C=O at 288.8 eV bonds [68]. In contrast, the XPS C 1 s peak of the rGO modified surface could be deconstructed into more components corresponding to various functional groups: sp²-hybridized carbon (C=C, 284.1 eV), sp³-hybridized carbon (C-C, 284.7 eV), hydroxyl (C-OH, 285.5 eV), epoxide (C-O-C, 286.2 eV), carbonyl (C=O, 287.5 eV), carboxyl (O-C=O, 288.8 eV) groups [69], and characteristic peaks of the nafion (CF_2 , 290.9 eV and CF_3 , 292.5 eV) [70]. From the XPS spectrum of the rGO modified surface, the presence of oxygen-containing functional groups can be revealed, although their intensity is notably lower than those observed on the 3D printed surface. While residual oxygen groups are not completely eliminated, they contribute to enhancing the interaction with biomolecules [71], thereby the rGO drop casting transform the electrode surface into a more bioactive surface compared to the 3D printed surface alone.

3.5. Electrochemical performance before and after rGO modification

The EIS technique is employed subsequently to assess the impedance of the 3D printed electrode surface and rGO modified surface in 1X PBS. The Nyquist plot of 3D printed electrode surface (figure 5(a) black) presents two semi-circles in the high-frequency and mid-frequency regions. The first semi-circle (high frequency) corresponds to the passive surface ($R_{\rm p}$), while the second semi-circle (mid-frequency) represents charge-transfer resistance ($R_{\rm ct}$) [72, 73]. The radiuses of these semi-circles provide the values of the $R_{\rm p}$ (170 Ω) and $R_{\rm ct}$ (330 Ω), offering insights into the electron-transfer kinetics at the electrode interface [74]. Consequently, an equivalent electrical circuits model for the 3D printed electrode surface is proposed (figure 5(b) top).

The proposed equivalent electrical circuit model for 3D printed electrode surface comprises of the electrolyte solution (PBS) resistance R_s , a constant phase element CPE1 with an impedance (Z_{CPE1}) which probably causes by the capacitance of the formed oxide products and pores on the rough solid surface of copper-polyester. The R_p within a formed pores or oxides on the solid surface is likely associated with the degradation of polyester [76] and the corrosion of copper [77]. The R_{ct} characterizes the polarization of

the copper-polyester due to the formation of the electric double layer on the interface between the copperpolyester and the PBS solution. A constant phase element CPE2 with impedance Z_{CPE2} which represent the capacitance of electrical double layer $(C_{\rm dl})$ on the interface between the copper-polyester and the PBS solution. From a physical interpretation standpoint, the current traverses the copper-polyester surface through ionic charge transfer [74]. This process results in either charge transfer across the interface (leading to corrosion and degradation) or charge storage at the interface, forming pores and oxides on the surface. These can be regarded as a passivation film. The emergence of this passivated impedance hampers charge transfer and reduces the surface's electrical conductivity. If the negative effects of this passivation film can be mitigated, the electroactive surface area could be expanded, thereby enhancing electron transport between the medium and the electrode.

To probe into the variations in interfacial properties, the EIS technique is also utilized to measure the impendence of rGO modified surfaces across a range of frequencies in PBS. Insights into the charge transfer dynamics and diffusion behavior in the rGO modified surfaces can be obtained from the Nyquist plots (figure 5(a) red). The presence of semicircles in the high-frequency domain corresponds $R_{\rm ct}$ (200 Ω), while the slope of the straight lines in the low-frequency region bears a linear relation to the ion diffusion coefficient [74], which contributes to the construction of an equivalent circuit of the rGO modified surface in PBS. This modeled circuit comprises four main components (figure 5(b) bottom): The R_s represents the ionic conduction, R_{ct} and C_{dl} symbolize the charge transfer at the rGO surface and the charging-discharging processes at double layers, respectively. The Warburg Impedance (W), a common circuit element employed for modeling diffusion behavior, illustrates the mass transport process in this context. Interestingly, the rGO coating appears to eliminate the passivated film impedance of the 3D printed electrode surface. It safeguards the printed electrode's surface from oxidation and degradation while simultaneously facilitating ion diffusion from the electrolyte to the sensor surface. Moreover, the R_{ct} for rGO modified electrode is approximately a mere 200 ohms. This value is significantly smaller than those reported in previous studies concerning graphene-based sensor [75, 78].

To evaluate the performance of FDM 3D printed sensors, we selected hydrogen peroxide detection as a demonstrative test. This choice is predicated on the exceptional catalytic properties of rGO in the presence of residual oxygen-containing groups, making it particularly well-suited for H₂O₂ detection. The hydroxyl, carbonyl, and carboxyl groups located at the edges of rGO are highly reactive and

2D Mater. 11 (2024) 045008 Y Dou et al

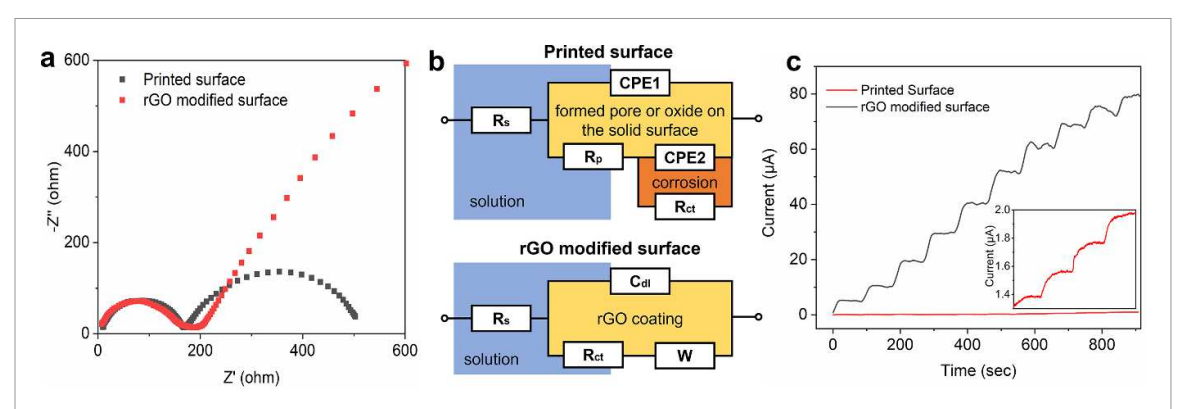


Figure 5. (a) Nyquist plot and (b) equivalent circuit derived from electrochemical impedance spectroscopy in 1X phosphate buffer solution for both 3D printed electrode surface and rGO modified surface. (c) Amperometric sensing of 0.1 M concentration increases (steps) of hydrogen peroxide with both 3D printed electrode and rGO modified electrode.

Table 2. The sensitivities of graphene-based H₂O₂ sensors with different fabrication and modification methods.

Process method	Materials	Electrode modification	Sensitivity	References
Inkjet printed graphene	rGO in terpineol/ cyclohexanone	UV-pulsed laser irradiation	39.9 mA·M ⁻¹ ·cm ⁻²	[27]
FDM 3D Printed graphene	Graphene/PLA	Prussian blue	$57.3 \text{ mA} \cdot \text{M}^{-1} \cdot \text{cm}^{-2}$	[51]
FDM 3D Printed graphene	Graphene/PLA	Prussian blue	$87 \text{ mA} \cdot \text{M}^{-1} \cdot \text{cm}^{-2}$	[52]
Drop casted graphene	rGO (modified Hummers' method)		$25 \text{ mA} \cdot \text{M}^{-1} \cdot \text{cm}^{-2}$	[75]
This work	Copper/polyester	Drop casted rGO (modified Hummers' method)	$156 \text{ mA} \cdot \text{M}^{-1} \cdot \text{cm}^{-2}$	

promote the breakdown of H2O2 into hydroxyl radicals. Additionally, the oxygen-containing groups on the basal plane of rGO, including hydroxyl and epoxide groups, facilitate the cleavage of H_2O_2 into O and H₂O molecules [79]. This dual functionality establishes the fundamental basis for rGO to be utilized as a hydrogen peroxide sensor. As shown in figure 5(c), the comparative analysis shows a significant enhancement in sensitivity during H₂O₂ detection on the rGO modified surface in comparison to the 3D printed surface. Weak response currents on the 3D printed surface can be attributed to the presence of copper oxide, which has a reducing effect on hydrogen peroxide [80]. After the application of rGO casting, it is clear that upon the addition of H_2O_2 , the response current of the rGO modified electrode exhibits a rapid increase, stabilizing at steady-state values. The sensitivity of H₂O₂ oxidation increases by approximately fortyfold, rising from 3.92 mA·M⁻¹·cm⁻² at 3D printed surface to 156 mA·M⁻¹·cm⁻² at rGO modified

Table 2 provides a comparative view of the manufacturing process and performance of our sensor electrode with other reported graphene-based sensors. Interestingly, the 3D printed electrode with rGO modification exhibits improved sensitivity relative to other graphene-based sensors. This distinction is primarily due to our rGO suspension not requiring

the integration of any non-conductive chemical components to enhance viscosity, as necessitated by technologies such as inkjet printing [27]. Consequently, the charge transfer resistance of the rGO modified electrode surface is diminished. Moreover, our approach contrasts with other FDM 3D printing methods that employ polymer/graphene to create the entire 3D structure of the electrodes. In our methodology, the 3D structure of the electrodes is printed using a highly conductive filament, with graphene modification limited to the electrode surface. This approach significantly reduces electron transfer resistance within the electrodes. In summary, compared to conventional forms, our rGO modified 3D printed electrode is more conducive to receiving and transmitting electrical signals, thereby enhancing overall performance. For instance, when compared to the rGO drop casting sensors' work, the 3D printed sensor displays five times the sensitivity with a similar rGO ink [75].

3.6. Influence of rGO thickness on sensor performance

To understand the variations in the roughness of 3D printed electrode surface and rGO modified electrode surface, we employ a wide-area, non-contact, and high-resolution 3D measurement system for the further investigation. Equipped with a camera mounted

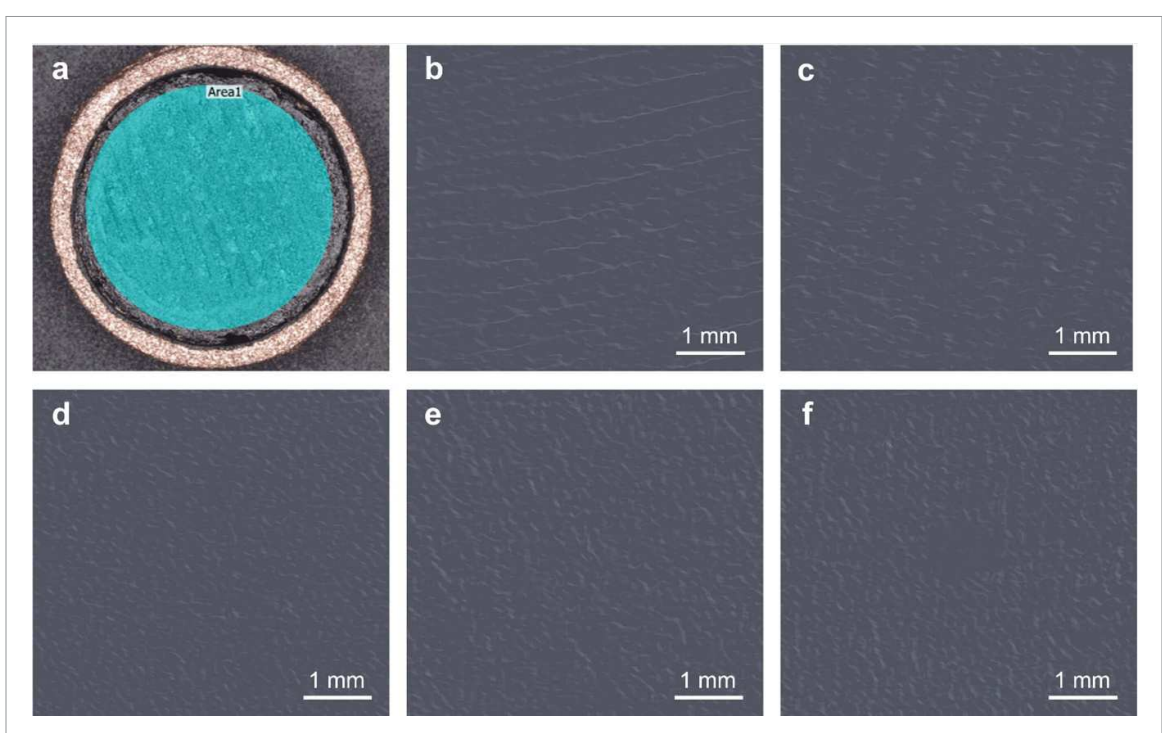


Figure 6. Wide-area 3D measurement system working schematic (a) and 3D models of the 3D printed electrodes surface without rGO modified (b) and with rGO modified at mass loading of 20 μ g (c), 40 μ g (d), 80 μ g (e), and 120 μ g (f) respectively.

directly above the sample, it captures the distortions in light bands due to alterations in the surface height of the sample, as shown in figure 6(a). These measured distortions are triangulated among varying patterns to construct a quantitative 3D model of surface topography. The captured images reveal that the electrode surface modified with 20 μ g rGO (figure 6(c)), still retains a discernible pattern of printed lines, similar to the 3D printed electrode surface (figure 6(b)). On the contrary, the trace left by the 3D printing process is absent on the surfaces of the electrodes modified with 40, 80, and 120 μ g rGO (figures 6(d), (e), and (f)). Notably, the electrodes modified with 40 μ g or more rGO display similarly uneven surfaces.

Table S1 presents the arithmetical mean height (S_a) and maximum height (S_z) of the electrode surfaces, as gathered from the wide-area 3D measurement system. The 3D printed electrode surface demonstrates a S_a of 0.025 mm and an S_z of 0.407 mm. However, upon the application of rGO coating, there is an increase in the S_a and S_z values to 0.033 and 0.962 mm respectively at 20 μ g, followed by a gradual decline to 0.012 and 0.101 mm at 120 μ g. The observed increase in S_a and S_z values when transitioning from the uncoated state to the 20 μ g rGO coated state implies effective dispersion of the 20 μ g rGO flakes on the rough electrode surface.

Not only does the right amount of rGO coating maintain the electrode's surface roughness, but it also contributes to a minor increase in the overall surface roughness. Subsequently, the declining S_a and S_z values on the rGO coated surface, as the coating increases from 20 to 120 μ g, indicate that an increasing number

of graphene sheets are stacking atop each other, leading to a gradual flattening of the electrode surface. These observations are congruent with the conclusions derived from the SEM results (figure S2), further strengthening the understanding of the correlation between rGO coating quantity and surface roughness of the electrode surface.

EIS measurements are employed to analyze the kinetic processes of ion diffusion and charge transfer at the electrode-electrolyte interface under different mass loadings of rGO. In the Nyquist plot (figure 7(a)), it is evident that the radius of the semicircle in the high-frequency range increases as the mass loading of rGO rises. This indicates that charge transfer becomes more facile with lower rGO coatings on the electrode surface. Moreover, the inverse correlation observed between the slope of the curve in the low-frequency range and the Warburg resistance, reflecting the ion diffusion process, underscores that lower mass loadings of rGO significantly enhance ion diffusion kinetics. This enhancement is attributed to the provision of a rougher surface texture and thinner layers of rGO. Also, an investigation into the relationship between sensitivity and the mass gradient of rGO modified sensor electrode is presented in figures 7(b) and (c). The sensitivity is found to be highest for the sensor electrode coated with 20 μ g of rGO. Beyond this point, an incremental increase in the coating mass results in a gradual decrease in sensitivity. Notably, the sensitivity of H_2O_2 oxidation at 120 μ g is approximately one-third of that observed at 20 μ g, dropping from 156 mA·M $^{-1}$ ·cm $^{-2}$ –52 mA·M $^{-1}$ ·cm $^{-2}$. When considering the 10 μ g sensor electrode, its sensitivity

IOP Publishing 2D Mater. 11 (2024) 045008 Y Dou et al

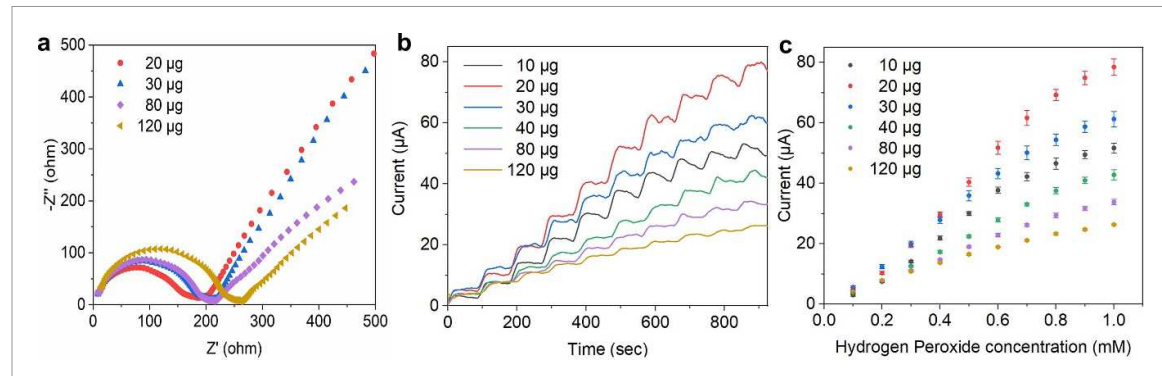


Figure 7. (a) Nyquist plot derived from electrochemical impedance spectroscopy in 1X phosphate buffer solution for rGO modified electrodes with different thickness of rGO. (b) Amperometric sensing of 0.1 M concentration increases (steps) of hydrogen peroxide with rGO modified sensors at distinct mass loading (10, 20, 30, 40, 80 and 120 μ g) and (c) corresponding linear regression analysis of the current versus concentration.

is inferior to that of the 20 μ g sensor electrode, due to the insufficiency of rGO mass to fully cover the electrode surface. The plot representing the current versus H₂O₂ concentration across all mass gradients, from 10 to 120 μ g, demonstrates a linear relationship within the range of 0.1–1 mM, and boasts a high correlation coefficient ($R^2 = 0.9824, 0.9876, 0.9932, 0.9972, 0.9956,$ and 0.9862).

4. Conclusion

This study introduces an innovative and scalable approach to electrochemical sensor fabrication utilizing FDM 3D printing technology. By employing a dual-extruder system, we seamlessly integrate conductive electrodes with insulating layers into a cohesive structure. This approach not only simplifies the fabrication process but also enhances the electrode's surface area through a deliberately roughened surface pattern. A key innovation in our method is the application of rGO casting, which markedly diminishes the electrode's charge transfer resistance and provides substantial protection against the oxidative degradation of materials. These enhancements contribute to the electrodes' exceptional electrocatalytic activity towards hydrogen peroxide detection. Our findings indicate that the efficiency of the rGOmodified sensors increases as the amount of rGO used decreases, with optimal performance achieved when the rough surface is completely covered. These promising results of this study advocate for the continued exploration and development of 3D printing technologies in sensor manufacturing, suggesting a fertile ground for future innovative research in this area.

Data availability statement

All data that support the findings of this study are included within the article (and any supplementary files).

Acknowledgments

This study is partially supported by NSF Grants CMMI-1826439 and CMMI-1762792. We also acknowledge the support from VivaGreen Limited and the use of facilities within the Eyring Materials Center at Arizona State University.

ORCID iDs

Kun Bi https://orcid.org/0000-0002-5217-0066 Qiong Nian https://orcid.org/0000-0003-4578-1253

References

- [1] Wang G, He X, Wang L, Gu A, Huang Y, Fang B, Geng B and Zhang X 2012 Non-enzymatic electrochemical sensing of glucose Mikrochim. Acta 180 161–86
- [2] Dong Q, Ryu H and Lei Y 2021 Metal oxide based non-enzymatic electrochemical sensors for glucose detection *Electrochim. Acta* 370 137744
- [3] Rassaei L, Marken F, Sillanpää M, Amiri M, Cirtiu C M and Sillanpää M 2011 Nanoparticles in electrochemical sensors for environmental monitoring *TRAC Trends Anal. Chem.* 30 1704–15
- [4] Tajik S, Beitollahi H, Garkani Nejad F, Dourandish Z, Khalilzadeh M A, Jang H W, Venditti R A, Varma R S and Shokouhimehr M 2021 Recent developments in polymer nanocomposite-based electrochemical sensors for detecting environmental pollutants *Ind. Eng. Chem. Res.* 60 1112–36
- [5] Lu L, Hu X, Zhu Z, Li D, Tian S and Chen Z 2019 Review—electrochemical sensors and biosensors modified with binary nanocomposite for food safety *J. Electrochem.* Soc. 167 037512
- [6] Mishra G K, Barfidokht A, Tehrani F and Mishra R K 2018 Food safety analysis using electrochemical biosensors Foods 7 141
- [7] Nemcekova K and Labuda J 2021 Advanced materials-integrated electrochemical sensors as promising medical diagnostics tools: a review *Mater. Sci. Eng.* C 120 111751
- [8] Mahato K and Wang J 2021 Electrochemical sensors: from the bench to the skin Sens. Actuators B 344 130178
- [9] Vasilescu A, Fanjul-Bolado P, Titoiu A-M, Porumb R and Epure P 2019 Progress in electrochemical (Bio)sensors for monitoring wine production *Chemosensors* 7 66
- [10] de Souza C C, Alves G F, Lisboa T P, Matos M A C and Matos R C 2022 Low-cost paper-based electrochemical

- sensor for the detection of ciprofloxacin in honey and milk samples *J. Food Compos. Anal.* **112** 104700
- [11] Zhou A A, Bai J, Hong W and Bai H 2022 Electrochemically reduced graphene oxide: preparation, composites, and applications Carbon 191 301–32
- [12] Karačić D, Gutić S J, Vasić B, Mirsky V M, Skorodumova N V, Mentus S V and Pašti I A 2022 Electrochemical reduction of thin graphene-oxide films in aqueous solutions—restoration of conductivity Electrochim. Acta 410 140046
- [13] Singh S, Pankaj A, Mishra S, Tewari K and Pratap Singh S 2019 Cerium oxide-catalyzed chemical vapor deposition grown carbon nanofibers for electrochemical detection of Pb(II) and Cu(II) J. Environ. Chem. Eng. 7 103250
- [14] Imran M, Kim E-B, Kwak D-H, Akhtar M S and Ameen S 2021 Controlled growth of WO₃ pyramidal thin film via hot-filament chemical vapor deposition: electrochemical detection of ethylenediamine *Chemosensors* 9 257
- [15] Liu B, Chen L, Liu G, Abbas A N, Fathi M and Zhou C 2014 High-performance chemical sensing using Schottky-contacted chemical vapor deposition grown monolayer MoS₂ transistors ACS Nano 8 5304–14
- [16] Li X, Zhao T, Wang K, Yang Y, Wei J, Kang F, Wu D and Zhu H 2011 Directly drawing self-assembled, porous, and monolithic graphene fiber from chemical vapor deposition grown graphene film and its electrochemical properties *Langmuir* 27 12164–71
- [17] Fruncillo S, Su X, Liu H and Wong L S 2021 Lithographic processes for the scalable fabrication of micro- and nanostructures for biochips and biosensors ACS Sens. 6 2002–24
- [18] Dhahi T S, Hashim U B, Ahmed N and Taib A M 2010 A review on the electrochemical sensors and biosensors composed of nanogaps as sensing material J. Optoelectron. Adv. Mater. 12 1857–62
- [19] Vivaldi F M, Dallinger A, Bonini A, Poma N, Sembranti L, Biagini D, Salvo P, Greco F and Di Francesco F 2021 Three-dimensional (3D) laser-induced graphene: structure, properties, and application to chemical sensing ACS Appl. Mater. Interfaces 13 30245–60
- [20] Moya A, Gabriel G, Villa R and Javier Del Campo F 2017 Inkjet-printed electrochemical sensors Curr. Opin. Electrochem. 3 29–39
- [21] Sui Y and Zorman C A 2020 Review—inkjet printing of metal structures for electrochemical sensor applications J. Electrochem. Soc. 167 037571
- [22] Liu X, Yao Y, Ying Y and Ping J 2019 Recent advances in nanomaterial-enabled screen-printed electrochemical sensors for heavy metal detection *TRAC Trends Anal. Chem.* 115 187–202
- [23] Yao Y, Wu H and Ping J 2019 Simultaneous determination of Cd(II) and Pb(II) ions in honey and milk samples using a single-walled carbon nanohorns modified screen-printed electrochemical sensor *Food Chem.* 274 8–15
- [24] Asaduzzaman M, Zahed M A, Sharifuzzaman M, Reza M S, Hui X, Sharma S, Do Shin Y and Park J Y 2023 A hybridized nano-porous carbon reinforced 3D graphene-based epidermal patch for precise sweat glucose and lactate analysis Biosens. Bioelectron. 219 114846
- [25] Ipekci H H, Gozutok Z, Celik N, Serdar Onses M and Uzunoglu A 2021 Ink-jet printing of particle-free silver inks on fabrics with a superhydrophobic protection layer for fabrication of robust electrochemical sensors *Microchem. J.* 164 106038
- [26] He Q, Das S R, Garland N T, Jing D, Hondred J A, Cargill A A, Ding S, Karunakaran C and Claussen J C 2017 Enabling inkjet printed graphene for ion selective electrodes with postprint thermal annealing ACS Appl. Mater. Interfaces 9 12719–27
- [27] Das S R, Nian Q, Cargill A A, Hondred J A, Ding S, Saei M, Cheng G J and Claussen J C 2016 3D nanostructured inkjet printed graphene via UV-pulsed laser irradiation enables paper-based electronics and electrochemical devices Nanoscale 8 15870–9

- [28] Aparicio-Martínez E, Ibarra A, Estrada-Moreno I A, Osuna V and Dominguez R B 2019 Flexible electrochemical sensor based on laser scribed Graphene/Ag nanoparticles for non-enzymatic hydrogen peroxide detection Sens. Actuators B 301 127101
- [29] Wang L, Zhang W, Samavat S, Deganello D and Teng K S 2020 Vertically aligned graphene prepared by photonic annealing for ultrasensitive biosensors ACS Appl. Mater. Interfaces 12 35328–36
- [30] Potts S-J, Lau Y C, Dunlop T, Claypole T and Phillips C 2019 Effect of photonic flash annealing with subsequent compression rolling on the topography, microstructure and electrical performance of carbon-based inks J. Mater. Sci. 54 8163–76
- [31] Garland N T, McLamore E S, Cavallaro N D, Mendivelso-Perez D, Smith E A, Jing D and Claussen J C 2018 Flexible laser-induced graphene for nitrogen sensing in soil ACS Appl. Mater. Interfaces 10 39124–33
- [32] Rocha D P, Squissato A L, da Silva S M, Richter E M and Munoz R A 2020 Improved electrochemical detection of metals in biological samples using 3D-printed electrode: chemical/electrochemical treatment exposes carbon-black conductive sites *Electrochim. Acta* 335 135688
- [33] Cardoso R M, Silva P R, Lima A P, Rocha D P, Oliveira T C, Do Prado T M, Fava E L, Fatibello-Filho O, Richter E M and Muñoz R A 2020 3D-printed graphene/polylactic acid electrode for bioanalysis: biosensing of glucose and simultaneous determination of uric acid and nitrite in biological fluids Sens. Actuators B 307 127621
- [34] Muñoz J and Pumera M 2020 Accounts in 3D-printed electrochemical sensors: towards monitoring of environmental pollutants *ChemElectroChem* 7 3404–13
- [35] Cheng T S, Nasir M Z M, Ambrosi A and Pumera M 2017 3D-printed metal electrodes for electrochemical detection of phenols Appl. Mater. Today 9 212–9
- [36] Browne M P, Redondo E and Pumera M 2020 3D printing for electrochemical energy applications *Chem. Rev.* 120 2783–810
- [37] Mubarak S, Dhamodharan D and Byun H-S 2023 Recent advances in 3D printed electrode materials for electrochemical energy storage devices *J. Energy Chem.* 81 272–312
- [38] Manzanares Palenzuela C L, Novotny F, Krupicka P, Sofer Z and Pumera M 2018 3D-printed graphene/polylactic acid electrodes promise high sensitivity in electroanalysis *Anal. Chem.* 90 5753–7
- [39] Browne M P, Novotny F, Sofer Z and Pumera M 2018 3d printed graphene electrodes' electrochemical activation ACS Appl. Mater. Interfaces 10 40294–301
- [40] Hamzah H H, Shafiee S A, Abdalla A and Patel B A 2018 3D printable conductive materials for the fabrication of electrochemical sensors: a mini review *Electrochem*. *Commun.* 96 27–31
- [41] Richter E M, Rocha D P, Cardoso R M, Keefe E M, Foster C W, Munoz R A A and Banks C E 2019 Complete additively manufactured (3D-printed) electrochemical sensing platform *Anal. Chem.* 91 12844–51
- [42] Bin Hamzah H H, Keattch O, Covill D and Patel B A 2018 The effects of printing orientation on the electrochemical behaviour of 3D printed acrylonitrile butadiene styrene (ABS)/carbon black electrodes Sci. Rep. 8 9135
- [43] Katseli V, Economou A and Kokkinos C 2019 Single-step fabrication of an integrated 3D-printed device for electrochemical sensing applications *Electrochem. Commun.* 103 100–3
- [44] Katseli V, Economou A and Kokkinos C 2020 A novel all-3D-printed cell-on-a-chip device as a useful electroanalytical tool: application to the simultaneous voltammetric determination of caffeine and paracetamol *Talanta* 208 120388
- [45] Honeychurch K C, Rymansaib Z and Iravani P 2018 Anodic stripping voltammetric determination of zinc at a 3-D printed carbon nanofiber–graphite–polystyrene electrode

- using a carbon pseudo-reference electrode Sens. Actuators B 267 476–82
- [46] Rymansaib Z, Iravani P, Emslie E, Medvidović-Kosanović M, Sak-Bosnar M, Verdejo R and Marken F 2016 All-polystyrene 3D-printed electrochemical device with embedded carbon nanofiber-graphite-polystyrene composite conductor *Electroanalysis* 28 1517–23
- [47] Silva T A, Moraes F C, Janegitz B C and Fatibello-Filho O 2017 Electrochemical biosensors based on nanostructured carbon black: a review J. Nanomater. 2017 1–14
- [48] Cardoso R M, Kalinke C, Rocha R G, Dos Santos P L, Rocha D P, Oliveira P R, Janegitz B C, Bonacin J A, Richter E M and Munoz R A A 2020 Additive-manufactured (3D-printed) electrochemical sensors: a critical review Anal. Chim. Acta 1118 73–91
- [49] Flowers P F, Reyes C, Ye S, Kim M J and Wiley B J 2017 3D printing electronic components and circuits with conductive thermoplastic filament Addit. Manuf. 18 156–63
- [50] Martins G, Gogola J L, Budni L H, Janegitz B C, Marcolino-Junior L H and Bergamini M F 2021 3D-printed electrode as a new platform for electrochemical immunosensors for virus detection *Anal. Chim. Acta* 1147 30–37
- [51] Rocha R G, Stefano J S, Cardoso R M, Zambiazi P J, Bonacin J A, Richter E M and Munoz R A A 2020 Electrochemical synthesis of Prussian blue from iron impurities in 3D-printed graphene electrodes: amperometric sensing platform for hydrogen peroxide *Talanta* 219 121289
- [52] Katic V, Dos Santos P L, Dos Santos M F, Pires B M, Loureiro H C, Lima A P, Queiroz J C M, Landers R, Munoz R A A and Bonacin J A 2019 3D printed graphene electrodes modified with prussian blue: emerging electrochemical sensing platform for peroxide detection ACS Appl. Mater. Interfaces 11 35068–78
- [53] Cruz M A, Ye S, Kim M J, Reyes C, Yang F, Flowers P F and Wiley B J 2018 Multigram synthesis of Cu-Ag core–shell nanowires enables the production of a highly conductive polymer filament for 3D printing electronics *Part. Part. Syst. Charact.* 35 1700385
- [54] Marcano D C, Kosynkin D V, Berlin J M, Sinitskii A, Sun Z, Slesarev A, Alemany L B, Lu W and Tour J M 2010 Improved synthesis of graphene oxide ACS Nano 4 4806–14
- [55] Justino C I, Gomes A R, Freitas A C, Duarte A C and Rocha-Santos T A 2017 Graphene based sensors and biosensors TRAC Trends Anal. Chem. 91 53–66
- [56] Schroeder V, Savagatrup S, He M, Lin S and Swager T M 2018 Carbon nanotube chemical sensors Chem. Rev. 119 599–663
- [57] Sinha A, Zhao H, Huang Y, Lu X, Chen J and Jain R 2018 MXene: an emerging material for sensing and biosensing TRAC Trends Anal. Chem. 105 424–35
- [58] Yang M, Li P H, Chen S H, Xiao X Y, Tang X H, Lin C H, Huang X J and Liu W Q 2020 Nanometal oxides with special surface physicochemical properties to promote electrochemical detection of heavy metal ions *Small* 16 2001035
- [59] Janata J and Josowicz M 2003 Conducting polymers in electronic chemical sensors Nat. Mater. 2 19–24
- [60] Ferri S, Kojima K and Sode K 2011 Review of glucose oxidases and glucose dehydrogenases: a bird's eye view of glucose sensing enzymes J. Diabetes Sci. Technol. 5 1068–76
- [61] Ahmed A, Singh A, Young S-J, Gupta V, Singh M and Arya S 2022 Synthesis techniques and advances in sensing applications of reduced graphene oxide (rGO) composites: a review Composites A 165 107373
- [62] Syrlybayev D, Zharylkassyn B, Seisekulova A, Akhmetov M, Perveen A and Talamona D 2021 Optimisation of strength

- properties of FDM printed parts-a critical review *Polymers*13 1587
- [63] Najmon J C, Raeisi S and Tovar A 2019 Additive Manufacturing for the Aerospace Industry (Elsevier) pp 7–31
- [64] Pimenta M, Dresselhaus G, Dresselhaus M S, Cancado L, Jorio A and Saito R 2007 Studying disorder in graphite-based systems by Raman spectroscopy *Phys. Chem. Chem. Phys.* 9 1276–90
- [65] Hidayah N M S, Liu -W-W, Lai C-W, Noriman N Z, Khe C-S, Hashim U and Lee H C 2017 Comparison on graphite, graphene oxide and reduced graphene oxide: synthesis and characterization AIP Conf. Proc. 1892 150002
- [66] Kaushal A, Dhawan S and Singh V 2019 Determination of crystallite size, number of graphene layers and defect density of graphene oxide (GO) and reduced graphene oxide (RGO) AIP Conf. Proc. 2115 030106
- [67] Wang D, Dai R, Zhang X, Liu L, Zhuang H, Lu Y, Wang Y, Liao Y and Nian Q 2020 Scalable and controlled creation of nanoholes in graphene by microwave-assisted chemical etching for improved electrochemical properties *Carbon* 161,880–91
- [68] Beamson G 1992 High relution XPS of organic polymers. The scienta ESCA 300 database ICIplc
- [69] Al-Gaashani R, Najjar A, Zakaria Y, Mansour S and Atieh M A 2019 XPS and structural studies of high quality graphene oxide and reduced graphene oxide prepared by different chemical oxidation methods *Ceram. Int.* 45 14439–48
- [70] Chen C, Levitin G, Hess D W and Fuller T F 2007 XPS investigation of Nafion® membrane degradation J. Power Sources 169 288–95
- [71] Carvalho A P G, Alegria E, Fantoni A, Ferraria A M, Do Rego A M B and Ribeiro A P C 2022 Effect of graphene vs. Reduced graphene oxide in gold nanoparticles for optical biosensors-a comparative study *Biosensors* 12 163
- [72] Bredar A R C, Chown A L, Burton A R and Farnum B H 2020 Electrochemical impedance spectroscopy of metal oxide electrodes for energy applications ACS Appl. Energy Mater. 3 66–98
- [73] Magar H S, Hassan R Y A and Mulchandani A 2021 Electrochemical impedance spectroscopy (EIS): principles, construction, and biosensing applications Sensors 21 6578
- [74] Bard A J, Faulkner L R and White H S 2022 Electrochemical Methods: Fundamentals and Applications (Wiley)
- [75] Zöpfl A, Sisakthi M, Eroms J, Matysik F-M, Strunk C and Hirsch T 2015 Signal enhancement in amperometric peroxide detection by using graphene materials with low number of defects Mikrochim. Acta 183 83–90
- [76] Fernández-Sánchez C, McNeil C J and Rawson K 2005 Electrochemical impedance spectroscopy studies of polymer degradation: application to biosensor development TRAC Trends Anal. Chem. 24 37–48
- [77] Luo J, Hein C, Pierson J-F and Mücklich F 2019 Localised corrosion attacks and oxide growth on copper in phosphate-buffered saline *Mater. Charact.* 158 109985
- [78] Vernardou D, Vasilopoulos K and Kenanakis G 2017 3D printed graphene-based electrodes with high electrochemical performance Appl. Phys. A 123 1–7
- [79] Gong B, Ku C, Yu H-Q and Sit P H-L 2022 Predicting the mechanisms for H₂O₂ activation and phenol oxidation catalyzed by modified graphene-based systems using density functional theory ACS Appl. Mater. Interfaces 14 35682–93
- [80] Song M J, Hwang S W and Whang D 2010 Non-enzymatic electrochemical CuO nanoflowers sensor for hydrogen peroxide detection *Talanta* 80 1648–52